Harnessing the Manifold Structure of Cardiomechanical Signals for Physiological Monitoring During Hemorrhage

Jonathan Zia [ID], *Student Member, IEEE*, Jacob Kimball [ID], *Student Member, IEEE*, Christopher Rozell [ID], *Senior Member, IEEE*, and Omer T. Inan [ID], *Senior Member, IEEE*

Abstract—*Objective:* Local oscillation of the chest wall in response to events during the cardiac cycle may be captured using a sensing modality called seismocardiography (SCG), which is commonly used to infer cardiac time intervals (CTIs) such as the pre-ejection period (PEP). An important factor impeding the ubiquitous application of SCG for cardiac monitoring is that morphological variability of the signals makes consistent inference of CTIs a difficult task in the time-domain. The goal of this work is therefore to enable SCG-based physiological monitoring during trauma-induced hemorrhage using signal dynamics rather than morphological features. *Methods:* We introduce and explore the observation that SCG signals follow a consistent low-dimensional manifold structure during periods of changing PEP induced in a porcine model of trauma injury. Furthermore, we show that the distance traveled along this manifold correlates strongly to changes in PEP ($\triangle$PEP). *Results:* $\triangle$PEP estimation during hemorrhage was achieved with a median R^2 of 92.5% using a rapid manifold approximation method, comparable to an ISOMAP reference standard, which achieved an R^2 of 95.3%. *Conclusion:* Rapidly approximating the manifold structure of SCG signals allows for physiological inference abstracted from the time-domain, laying the groundwork for robust, morphology-independent processing methods. *Significance:* Ultimately, this work represents an important advancement in SCG processing, enabling future clinical tools for trauma injury management.

Index Terms—Seismocardiogram, manifold, ISOMAP, pre-ejection period, signal quality.

I. INTRODUCTION

SINCE its early description in the 1960 s, the seismocardiogram (SCG) has emerged as a promising sensing modality for the noninvasive assessment of cardiomechanical function [1].

Jonathan Zia is with the School of Electrical and Computer Engineering, Georgia Institute of Technology, Atlanta, GA 30332 USA (e-mail: zia@gatech.edu).

Jacob Kimball, Christopher Rozell, and Omer T. Inan are with the School of Electrical and Computer Engineering, Georgia Institute of Technology.

Typically captured using chest-mounted inertial measurement units, the SCG measures local oscillation of the chest wall occurring in response to underlying hemodynamic events [2]. Prior literature has demonstrated a strong relationship between time-domain features of the SCG signal and cardiac time intervals (CTIs), most notably the pre-ejection period (PEP) and left ventricular ejection time (LVET), essential indicators of cardiac preload and contractility [3], [4]. Coupled with the advent of wearable microelectronics, such physiological insights suggest that the SCG may enable cardiac monitoring systems of the future to assess cardiomechanical function noninvasively [5]–[7]. This would prove invaluable for the diagnosis and management of diseases which affect cardiomechanical function, from chronic illnesses such as heart failure [8] and hypertension [9], [10] to acute conditions such as ischemic events [11] and hemorrhage [12].

In particular, the focus of this work is physiological monitoring during hemorrhage and subsequent fluid resuscitation via PEP estimation, one of several key indicators of cardiomechanical function. Hemorrhage is a common complication of trauma injury, which accounted for 5 million deaths globally in the year 2000 at an economic burden of $117 billion in the U.S. alone [13]. For patients suffering from trauma-induced hemorrhage, timely and appropriate care are essential for preventing hypovolemic shock, which comprises the majority of preventable fatalities [14]. As an estimated 1 in 4 trauma fatalities are preventable, it is incumbent upon healthcare providers to rapidly assess the severity of hemorrhage and titrate care appropriately [15]. Toward the development of clinical tools to aid healthcare providers, recent literature has indicated that tracking cardiomechanical indicators such as PEP via SCG may enable providers to track the progression of hemorrhage and provide individualized treatment [12], [16].

A significant limitation which has prevented the ubiquitous application of SCG technology is the morphological variability of the signals, which is highly patient-specific, transient, and dependent upon sensor placement [2], [17]. This makes it difficult to consistently extract time- and frequency-domain features of the signal for PEP estimation [18], [19]. Even so, prior literature has typically focused on identification and extraction of time-domain features in spite of this variability, which may then be related to PEP [17]. Though such approaches have demonstrated success in PEP estimation, they are inherently
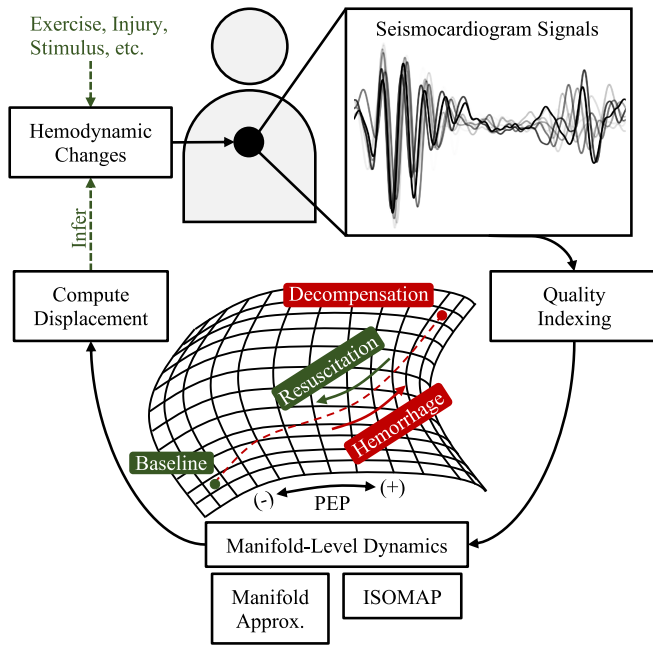
Fig. 1. Overview of this work. Hemodynamic changes such as modulation of PEP are reflected in the SCG signal. After an initial step of quality indexing to remove noisy signals, the remaining SCG signals are confined to a low-dimensional manifold. The distance traveled by the signal along the manifold may be used to infer changes in hemodynamic indicators such as PEP in a manner that is abstracted from time-domain features.

subject to the transient time-frequency characteristics of the signal.

The goal of this work is to introduce an approach to PEP estimation from SCG signals which is abstracted from the time-domain, focusing instead on the *inherent dynamics* of the signal. Namely, we will demonstrate that SCG signals exhibit a consistent low-dimensional manifold structure during periods of hemodynamic change, and that displacement along the manifold is linearly-related to changes in PEP. To obtain an accurate estimate of displacement along the manifold, we begin by using the classic ISOMAP algorithm; however, as this approach is computationally complex and thereby impractical for wearable systems, we then show that high performance may still be achieved with a rapid manifold approximation approach [20]. Manifold approximation algorithms have historically be used to map data to nonlinear subspaces in an efficient yet robust manner [21].

The overall process proposed in this work is illustrated in Fig. 1; SCG signals are first obtained from a chest-mounted accelerometer during periods of hemodynamic change. In this study, changes in PEP are induced via simulated hemorrhage and fluid resuscitation in a porcine animal model. The critical benefit of using a porcine model in this work is that (1) large changes in blood volume could be induced, better simulating clinical use-cases while closely approximating human cardiovascular physiology [22]; and (2) this allowed for collecting gold-standard measurements of PEP from direct cardiac catheterization [23], [24]. To estimate these induced changes in PEP, the first step is to remove low-quality signals using a signal quality index

(SQI). Following this, the SCG signals are nonlinearly-mapped to positions on a low-dimensional manifold, which may in turn be linearly-mapped directly to changes in PEP.

This manuscript is organized as follows. We begin by describing the experimental protocol, in which changes in PEP are induced in a porcine animal model. After formulating the quality indexing and manifold mapping methods used in this work, the relationship between manifold displacement and changes in PEP are analyzed. Ultimately, inferring cardiomechanical indicators such as PEP in a manner that is abstracted from the time-domain may serve as a harbinger for robust, morphology-independent methods of both processing and understanding SCG signals. Doing so represents a critical step in enabling reliable noninvasive monitoring of cardiomechanical function in clinical and outpatient environments using SCG. Specifically, the contributions of this work include:

1) Demonstrating that SCG signals exhibit a low-dimensional manifold structure during complex physiological processes such as changes in blood volume;
2) Inferring changes in PEP from these manifolds, abstracting SCG processing from the time domain.

II. METHODS

A. Experimental Protocol and Hardware

The following experimental protocol was conducted with approval from the Institutional Animal Care and Use Committees (IACUC) of the Georgia Institute of Technology, Translational Training and Testing Laboratories Inc. (T3 Labs), and the Department of the Navy Bureau of Medicine and Surgery (BUMED) and included six Yorkshire swine (3 castrated male, 3 female, Age: 114–150 days, Weight: 51.5–71.4 kg) undergoing induced hypovolemia followed by fluid resuscitation. Anaesthesia was first induced in the animal with xylazine and telazol and maintained with inhaled isoflurane during mechanical ventilation, and intravenous heparin was administered to prevent the coagulation of blood during the protocol. The animals' total blood volume was estimated using Evans blue dye administration [25], [26], following which hypovolemia was induced by draining blood passively through an arterial line into a sterile container at up to four levels of blood volume loss (BVL): 7%, 14%, 21%, and 28% [27]. Following each level of blood loss, exsanguination was paused for approximately 5-10 minutes to allow the cardiovascular system to stabilize. The procedure was followed until a safety threshold was reached, namely a 20% drop in mean arterial pressure (MAP). Upon reaching this threshold, fluid resuscitation was performed by re-infusing the stored blood through the arterial line at the same levels of blood volume loss, pausing again for 5-10 minutes between each level. Fig. 2(a) shows the PEP derived from the aortic root catheter during the experimental protocol for Pig 1, the calculation of which will be detailed below.

During the experiment, aortic root pressure was recorded by inserting a fluid-filled catheter through a vascular introducer in the right carotid artery. The vascular introducer was connected via a pressure monitoring line to an ADInstruments MLT0670 pressure transducer (ADInstruments Inc., Colorado Springs,
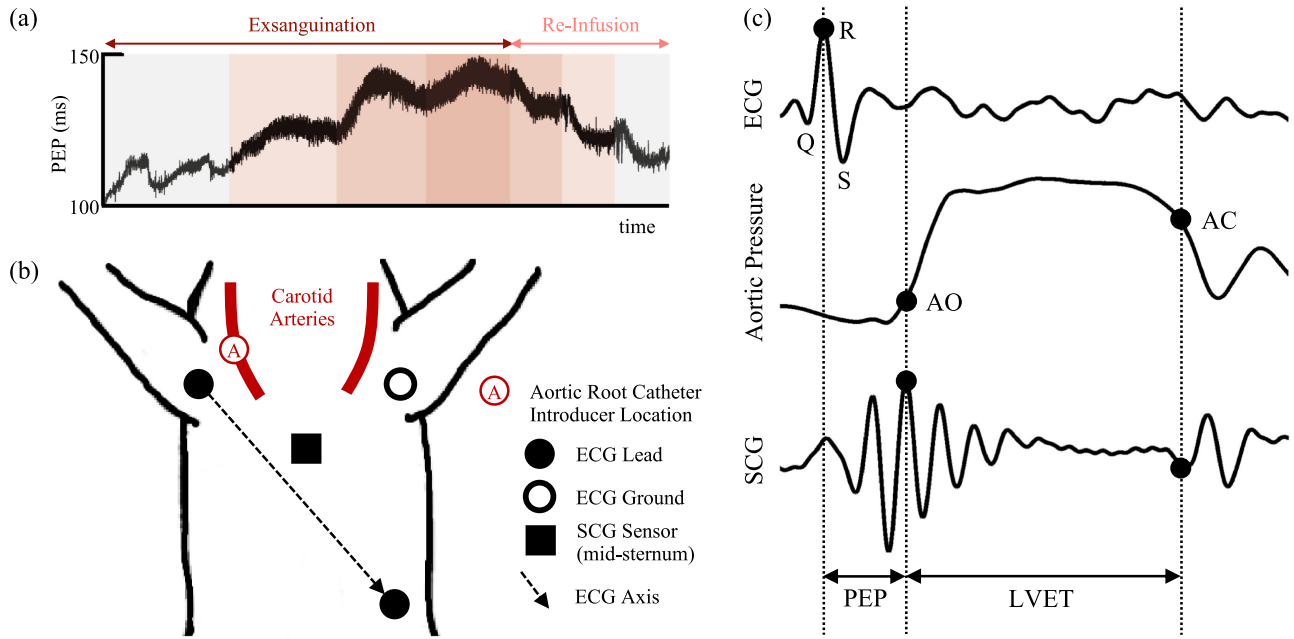
Fig. 2. (a) The PEP computed for each heartbeat during the protocol from the aortic pressure waveform of Pig 1. Darker red shading indicates higher blood volume loss (7%, 14%, and 21% respectively). (b) Sensor setup for the experimental protocol. ECG sensors are configured in Einthoven Lead II configuration. (c) Tracings from an example heartbeat from Pig 1. The ECG QRS complex is labeled along with the AO point derived from the aortic pressure waveform. As shown, the ECG R-peak and AO points are used to compute the PEP. The corresponding point on the SCG signal is labeled for illustration, though SCG feature points were not used for AO estimation in this work. Prior studies have used SCG signals to compute LVET as well via AC estimation, since the second high-energy complex of the SCG has been shown to correspond with the onset of diastole [4]; an example is provided in the figure for illustration, though LVET is not explored in this work.

CO, USA), with pressure data continuously recorded with an ADInstruments Powerlab 8/35 data acquisition system (DAQ) sampling at 2 kHz. Concurrent electrocardiogram (ECG) and SCG data was also captured using a wearable sensing system. As will be described, ECG was collected in order to segment the SCG signal on a heartbeat-by-heartbeat basis. ECG signals were captured using a three-lead system of adhesive-backed Ag/AgCl electrodes interfacing with a BIOPAC ECG100 C amplifier. SCG signals were captured using an ADXL354 accelerometer (Analog Devices, Inc., Norwood, MA, USA) placed on the mid-sternum, interfacing with a BIOPAC HLT100 C transducer interface module. Signals from these sensors were continuously recorded using a BIOPAC MP160 DAQ (BIOPAC Systems, Inc., Goleta, CA, USA) sampling at 2 kHz. A 1 Hz square wave output from the BIOPAC and fed into the Powerlab in order to commence recording simultaneously and ensure that both systems remained synchronized throughout the experiment. The configuration of the sensing system is detailed in Fig. 2(b).

B. Signal Pre-Processing

Only the dorso-ventral axis of SCG acceleration was used in this study [2]. All signals were first filtered with finite impulse response (FIR) band-pass filters with Kaiser window, both in the forward and reverse directions. Cutoffs were 0.5–40 Hz for the ECG, 1–40 Hz for the SCG [17], and 0.5–10 Hz for the aortic pressure signal [28]. Subsequently, the SCG and aortic pressure waveforms were segmented using the ECG R-peaks as

a reference. The resulting signal segments were abbreviated to a length of 1,000 samples (500 ms) from the R-peak, since this was shorter than the shortest R-R interval in the protocol while remaining long enough to capture systolic ejection. All SCG signals were then amplitude-normalized with mean-centering and unit variance.

The interval between the ECG R-peak and aortic opening (AO) is typically used as the PEP reference value [29], [30]. As illustrated in Fig. 2(c), AO was estimated from the aortic pressure waveform as the point of maximum second derivative, indicating the onset of the pressure upswing associated with systolic ejection; as the signals were R-peak-separated, the time elapsed from the beginning of each signal segment to the AO point was itself the PEP interval for each respective heartbeat. All processing in this work was performed with MATLAB 2018b (The Mathworks, Inc., Natick, MA, USA).

As it pertains to the assessment of arterial pressure and CTIs, catheter-based systems allow for the direct measurement of pressure gradients and the changes thereof during the cardiac cycle. Though infrequently used to measure PEP due to the difficulty in obtaining these signals, the relationship between AO and the upstroke of the arterial pressure waveform has long been established [24]. For this reason, cardiac catheterization was selected as the reference standard for PEP in this work. Notably, impedance cardiography (ICG) is another common method of estimating CTIs, however recent literature has suggested that ICG itself may be prone to considerable error and it was therefore not used as a reference standard in this work [31], [32].

Animal	Max BVL	No. of Instances
Pig 1	21%	18,916
Pig 2	28%	16,985
Pig 3	21%	10,956
Pig 4	21%	9,210
Pig 5	14%	13,400
Pig 6	28%	16,146

C. Notation

The matrix $\boldsymbol{X}_i \in \mathbb{R}^{M \times N}$ denotes the row-wise matrix of M SCG signals of length N for Pig i, such that $\boldsymbol{X}_i = \{\boldsymbol{x}_1, \boldsymbol{x}_2, \ldots, \boldsymbol{x}_M\}$. The vector $\boldsymbol{p}_i \in \mathbb{R}^M$ contains the catheter-derived PEP values for each signal in $\boldsymbol{X}_i$. In general, the subscript i indicates that the matrix or vector belongs to Pig i. The matrix $\boldsymbol{X}_{\bar{i}}$ denotes the row-wise matrix of SCG signals for all animal subjects excluding Pig i; $\boldsymbol{p}_{\bar{i}}$ therefore contains the PEP values for each signal in $\boldsymbol{X}_{\bar{i}}$. The notation $\boldsymbol{x}_j \in \boldsymbol{X}_i$ denotes the jth row (or, signal segment) in $\boldsymbol{X}_i$.

D. Signal Quality Indexing

Once segmented SCG signals and corresponding AO reference values for each heartbeat were obtained, the final step of pre-processing was to remove low-quality signals. To do so, the SQI previously developed in [33] was used. As described, the SQI of each SCG signal segment $\boldsymbol{x} \in \mathbb{R}^N$ was defined based on its distance from a template $\boldsymbol{t} \in \mathbb{R}^N$ via

$$SQI(\boldsymbol{x}, \boldsymbol{t}) = \exp \frac{-\lambda \mathscr{D}(\boldsymbol{x}, \boldsymbol{t})}{\mathscr{L}(\boldsymbol{x}, \boldsymbol{t})} \qquad (1)$$

where λ is a decay factor, $\mathscr{D}(\cdot)$ is a distance function and $\mathscr{L}(\cdot)$ is the length of the signals after distance calculation. In this manner, smaller values of distance resulted in an SQI near 1, and large values resulted in an SQI near 0. λ was set to 25 in this study as suggested in [33]; note that while this changes the numerical range of SQI values, it does not change the rank-ordering of signal quality, and thus changing this value to another positive-valued real number would not affect the results of this work. The distance metric used in this work was the dynamic time warping (DTW) algorithm, a ubiquitous method of estimating the distance between signals which computes the minimum Euclidian distance after stretching and compressing them in the time-domain [34]. Though [33] imposed additional constraints on the DTW algorithm, this work imposed only the fundamental constraints, as will be detailed below. Therefore, the function $\mathscr{D}(\cdot)$ in Equation 1 returned the distance between the warped signals, and $\mathscr{L}(\cdot)$ returned the length of the signals after warping.

The following processing was then performed separately for each animal. The first 100 SCG signal segments during the pre-hypovolemic baseline period were averaged elementwise to form a template $\boldsymbol{t}_i$ for the ith animal. Subsequently, the SQI was calculated for each SCG segment $\boldsymbol{x}_j \in \boldsymbol{X}_i$ via Equation 1, and the signals were ranked in order based on their SQI scores. A percentile threshold was then set on the scores, and the signals which fell below the threshold were removed from subsequent

processing. An example is shown in Fig. 3, in which the bottom 2% of SCG signals are highlighted and removed for the data from Pig 1 ($\boldsymbol{X}_1$). For visualization purposes, principal component analysis (PCA) was performed on the matrix $\boldsymbol{X}_1$, and the first three principal components (PCs) were plotted.

E. Nonlinear Dimensionality Reduction

Formally, manifolds are topological spaces which are locally Euclidian, or approximately flat on small regions of their surface [35]. When the intrinsic dimensionality of a dataset — or, the number of latent or hidden variables — is lower than the number of dimensions in the observed feature space, a common result is that the data forms a lower-dimensional manifold embedded in the higher-dimensional feature space. Less formally, the data may be constrained to a low-dimensional subspace of the original feature space, though the subspace may be curved and nonlinear. In these cases, it is desirable to re-embed the manifold in a feature space closer to its intrinsic dimensionality to enable more robust processing. Ideally, the dimensions of the new feature space may correspond to latent variables in the data, though this is not always a straightforward task. When the relationship between the latent and observed variables is approximately linear, linear dimensionality reduction techniques such as PCA are commonly used to identify a suitable subspace; otherwise, nonlinear methods may be more suitable for identifying these more complex, curved subspaces.

A classic technique for learning and re-embedding manifolds is the ISOMAP algorithm, the steps of which are illustrated in Fig. 4(a)–(c) for the data in Fig. 3. This algorithm is composed of three parts [20]:

1) **Graph Creation:** A graph is constructed from a sub-sampling of points $\boldsymbol{G}_i = \{\boldsymbol{g}_1, \boldsymbol{g}_2, \ldots, \boldsymbol{g}_L\}$ from the overall dataset $\boldsymbol{X}_i = \{\boldsymbol{x}_1, \boldsymbol{x}_2, \ldots, \boldsymbol{x}_M\}$, which form the nodes of the graph. A connection between nodes $\boldsymbol{g}_j$ and $\boldsymbol{g}_k$ are formed if and only if there exists a point $\boldsymbol{x}_\ell$ in the original dataset whose nearest neighbors are $\boldsymbol{g}_j$ and $\boldsymbol{g}_k$ as per the Euclidian distance.

2) **Geodesic Distance Estimation:** The geodesic distance between each pair of nodes $\boldsymbol{g}_j, \boldsymbol{g}_k \in \boldsymbol{G}_i$ is estimated by computing the shortest path between each pair of nodes that traverses the graph's connections. In this work, this is performed with the Floyd-Warshall algorithm [36].

3) **Manifold Re-Embedding:** The goal of this step is to learn a mapping $f : \mathbb{R}^{L \times N} \to \mathscr{Y}$ from the observation space of $\boldsymbol{G}_i$ to a lower-dimensional space $\mathscr{Y} = \mathbb{R}^{L \times D}$ which preserves the geodesic distances between pairs of points in the graph. In this work, we employ "classical" multidimensional scaling (MDS) to learn this mapping [37]. Specifically, MDS minimizes the loss function

$$L(f, \boldsymbol{G}_i) = \left(\frac{\sum_{j,k} \left(d_Y^{jk} - d_G^{jk} \right)^2}{\sum_{j,k} \left(d_Y^{jk} \right)^2} \right)^{1/2}, \qquad (2)$$

where $d_Y^{jk} = \|f(\boldsymbol{g}_j) - f(\boldsymbol{g}_k)\|_2$ is the Euclidian distance (or the ℓ_2-norm) between $f(\boldsymbol{g}_j)$ and $f(\boldsymbol{g}_k)$ in the output
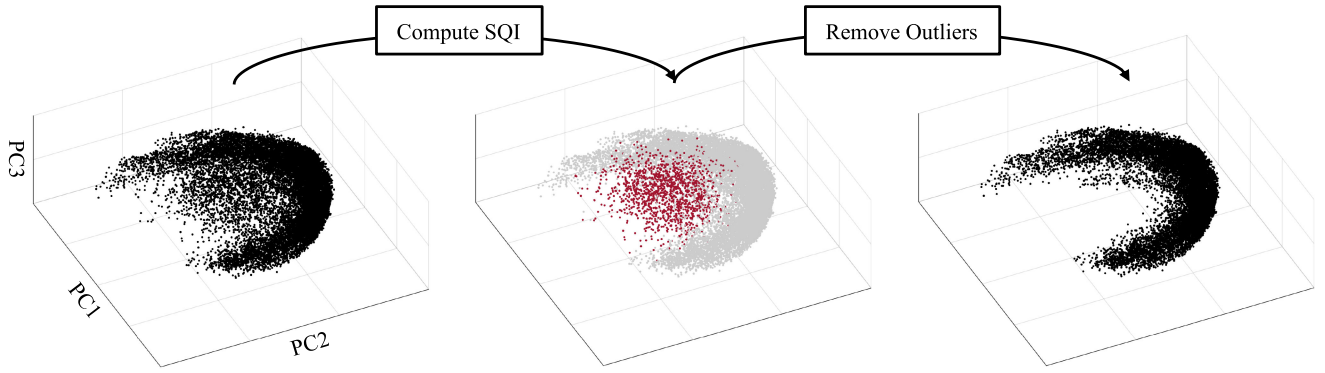
Fig. 3. Outlier identification and removal for the SCG data from Pig 1. Points highlighted in red represent the bottom 2% of SCG signals as per the SQI. Data is visualized in the first three PCA dimensions.

space $\mathcal{Y}$ and d_G^{jk} is the estimated Euclidian distance between the feature vectors $\boldsymbol{g}_j$ and $\boldsymbol{g}_k$ [37].

To obtain an accurate embedding of SCG manifolds the SQI was first applied to the data from each animal to remove outliers. The cutoff was increased in increments of 5% from 0% to 20% to observe the effects of the SQI on the performance of this method. 10% of the remaining signals were then randomly selected to form the set $\boldsymbol{G}_i$ as in [20]. The above algorithm was then performed to compute the geodesic distance between each pair of nodes, and MDS was used to map each point in $\boldsymbol{G}_i$ to a two-dimensional subspace $\mathcal{Y} = \mathbb{R}^{L \times 2}$. This resulted in obtaining the vectors $\boldsymbol{y}_i^{(1)}$ and $\boldsymbol{y}_i^{(2)} \in \mathbb{R}^L$, corresponding to the mapping of each point in $\boldsymbol{G}_i$ to the two dimensions of $\mathcal{Y}$ respectively. In this work, $\boldsymbol{y}_i^{(1)}$ was defined as the dimension which contained the larger variance, as shown in Fig. 4(c). Two dimensions were chosen based on the observation that the SCG manifolds were two-dimensional for all subjects, as will be shown subsequently in Fig. 5. Fig. 4 provides an overview of this process for Pig 1. As the final step of processing, the latent variable $\Delta \boldsymbol{y}$ was obtained for each animal by computing the offset of each element in $\boldsymbol{y}_i^{(1)}$ from the initial element in the vector $y_i^{(1)}(0)$, such that $\Delta \boldsymbol{y}_i = \boldsymbol{y}_i^{(1)} - y_i^{(1)}(0)$. This was done in order to obtain the displacement of each point on the manifold rather than the absolute position. As will be detailed later, this latent variable was then used to estimate the change in PEP (ΔPEP) via linear regression.

Fig. 4(a) shows the data from Pig 1 after a 10% cutoff was applied using the SQI. Note that while the data is plotted in the first three PCA dimensions, PCA was used for visualization purposes only with regards to ISOMAP. Fig. 4(b) shows the result of graph creation, and Fig. 4(c) shows the resulting mapping of the nodes of $\boldsymbol{G}_1$ to the two-dimensional subspace $\mathcal{Y}$. This process was repeated independently for all animals in the protocol.

F. Manifold Approximation

There are several drawbacks to using ISOMAP for manifold mapping. Estimating geodesic distance between each pair of points is a computationally-intensive process; for instance, the Floyd-Warshall algorithm has $O(N^3)$ complexity, though there exist slightly more efficient algorithms. Furthermore, ISOMAP

is highly-sensitive to outliers, as these may create skip-junctions across the manifold during graph creation, invalidating the calculated geodesic distance.

For practical application in wearable systems, we propose a simple manifold approximation algorithm for comparison to ISOMAP, illustrated in Fig. 4(d) and (e). Fig. 4(d) shows the data from all six animals, each with a different color, after applying the SQI with a cutoff of 10%. The data from all animals was combined to learn a single PCA transformation for plotting all the data on the same axes.

Since data from all animals exhibited consistent rotational dynamics, a simple manifold approximation could be performed, as illustrated in Fig. 4(e). For each animal, a separate PCA transformation was learned from the data from the remaining five animals ($\boldsymbol{X}_{\bar{i}}$) and applied to the data from the held-out animal ($\boldsymbol{X}_i$). The initial sample from the Pig i was then mapped to the nearest point on a unit circle in the plane of PC1 and PC2, centered at the origin. Each subsequent point was then also mapped to the nearest point on the unit circle, and the angular offset between the new point and the initial point was recorded. This resulted in a vector $\Delta \boldsymbol{\theta}_i$ containing the angular offset for each SCG signal in $\boldsymbol{X}_i$. This process is illustrated in Fig. 4(e), and was also repeated with an SQI cutoff increasing from 0% to 20% in increments of 5%.

As will be detailed, the latent variable $\Delta \boldsymbol{\theta}$ was then used to estimate ΔPEP in an analogous manner to $\Delta \boldsymbol{y}$ from ISOMAP. Unlike the ISOMAP algorithm, the manifold approximation algorithm has $O(N)$, and is thereby much more rapid; this enabled performing the analysis on all available datapoints rather than a sub-sampling. The total computation time of the ISOMAP algorithm for all subjects was 16 minutes on a 3.6 GHz Intel Core i7 7820X processor despite sampling 10% of the available SCG signal segments; the corresponding time was 33 seconds for the manifold approximation algorithm despite sampling all available segments.

G. Estimating Changes in Pre-Ejection Period

To determine whether there existed a relationship between SCG manifolds and PEP, we began by visualizing trends in the data. For each animal, the SCG data was combined to form a matrix $\boldsymbol{X}_i \in \mathbb{R}^{M \times N}$ after removing outliers with an SQI
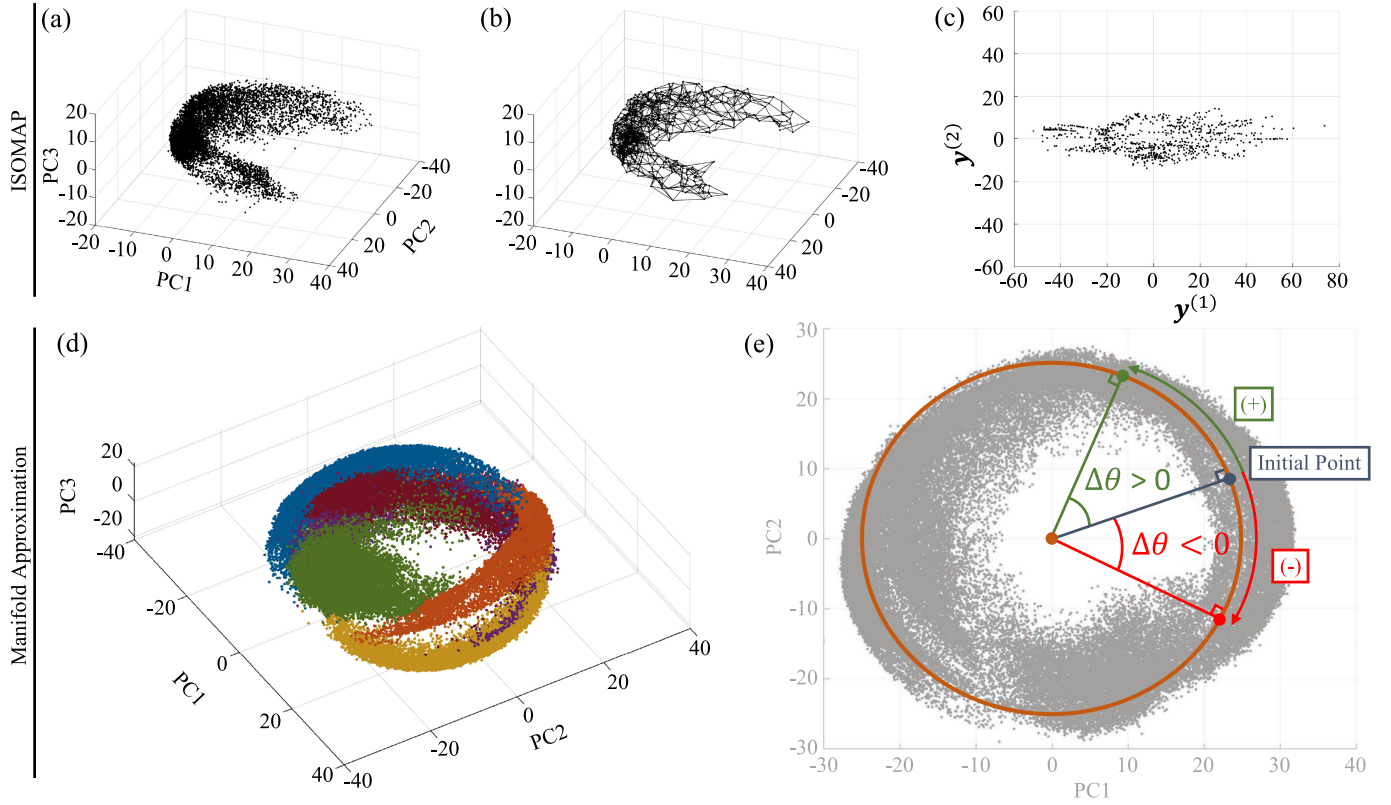
Fig. 4.   (a) Data from Pig 1 over the entire protocol after removing outliers with an SQI cutoff of 10%. (b) Illustration of the graph creation step of ISOMAP. (c) The manifold in (b) mapped to a two-dimensional subspace using classical MDS. (d) Data from all animal subjects after removing outliers with an SQI cutoff of 10% and applying the same PCA transformation to all subjects. Colors correspond to the different animals (Pig 1 = blue; Pig 2 = green; Pig 3 = orange; Pig 4 = purple; Pig 5 = red; Pig 6 = gold). (e) Manifold approximation process overlaid on data from (d). The initial datapoint in the experiment (blue) for each animal was mapped to a point on the reference circle (orange). Each subsequent point was then mapped to the circle, with its angular displacement relative to the initial point (positive = green; negative = red) recorded. Note that a unit circle was used in this study, though a large circle is shown here.

cutoff of 10%. The data was visualized by performing PCA on the matrix $\boldsymbol{X}_i$, and datapoints were shaded based on the PEP magnitude. Gradations in shading corresponding to a particular axis of the resulting manifold would suggest a relationship between the latent variables of the manifold and PEP which may be estimated with manifold mapping.

Following this step, we would like to determine the extent to which changes in the latent variables obtained from manifold mapping correlate with changes in PEP. Regarding the ISOMAP method, the latent variable of interest is $\Delta\boldsymbol{y}$, which was obtained for each subject upon performing MDS on the graph nodes. Regarding the proposed manifold approximation, the variable of interest is the offset $\Delta\boldsymbol{\theta}$. For each animal, the vector $\Delta\boldsymbol{p}_i$ denoting ΔPEP was first computed by subtracting each element of the vector of ground-truth PEP values $\boldsymbol{p}_i$ from the initial value $p_i(0)$, namely $\Delta\boldsymbol{p}_i = \boldsymbol{p}_i - p_i(0)$. The coefficient of determination (R^2) was determined between $\Delta\boldsymbol{y}_{\text{tot}}$ and $\Delta\boldsymbol{\theta}_{\text{tot}}$ — or, the vectors $\Delta\boldsymbol{y}_i$ and $\Delta\boldsymbol{\theta}_i$ concatenated across all animals — and the corresponding changes in PEP $\Delta\boldsymbol{p}_{\text{tot}}$ after again applying an SQI cutoff of 10% [38].

To yield more insight on the accuracy of these methods, ΔPEP was estimated using leave-one-subject-out cross validation (LOSO-CV) for both the ISOMAP and manifold approximation methods, and was performed separately for each SQI

cutoff. For ISOMAP, ΔPEP was estimated from $\Delta\boldsymbol{y}$; for each animal, a vector $\Delta\boldsymbol{y}_{\bar{i}}$ was created which contained the values of $\Delta\boldsymbol{y}$ for the remaining five animals in the study. This vector was regressed to the corresponding vector of ΔPEP values $\Delta\boldsymbol{p}_{\bar{i}}$ for each datapoint in $\Delta\boldsymbol{y}_{\bar{i}}$ using least squares regression of the form

$$\boldsymbol{\beta}_i = \underset{\hat{\boldsymbol{\beta}}}{\text{argmin}} \|\Delta\boldsymbol{p}_{\bar{i}} - \Delta\boldsymbol{y}_{\bar{i}}\hat{\boldsymbol{\beta}}\|_2^2 \qquad (3)$$

where $\boldsymbol{\beta}_i$ is the learned parameterization. This linear regression was then applied to the values of $\Delta\boldsymbol{y}_i$ for the held-out animal, and the root-mean-square error (RMSE) between true and estimated ΔPEP was recorded for each animal [38]. This process was repeated for the manifold approximation method, however the regression was learned between $\Delta\boldsymbol{\theta}$ and $\Delta\boldsymbol{p}$.

III. RESULTS AND DISCUSSION

A. Estimating Changes in Pre-Ejection Period

The manifolds formed by SCG signals during the experimental protocol are shown in Fig. 5(a)–(f) for each of the six animals respectively. In the PCA dimensions pictured, it is apparent that a similar two-dimensional semicircular manifold was preserved across all animals in the study. Furthermore, color gradation is present across the major axis of the manifold, which
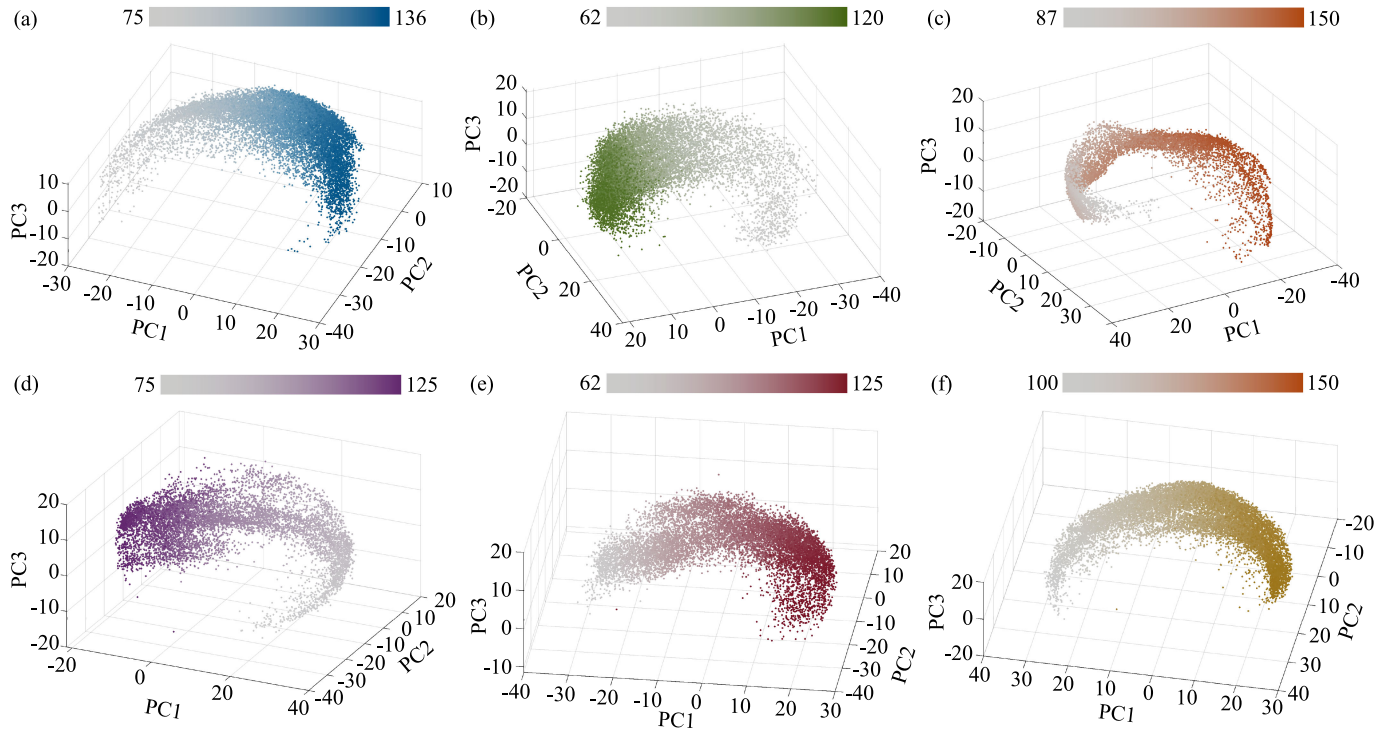
Fig. 5. (a)–(f) Data from Pigs 1–6 respectively plotted on first 3 PCA dimensions, with transformations computed separately for each animal. Shading corresponds to PEP, with darker shading indicating larger PEP. Colorbars are shown for each animal, indicating PEP in milliseconds.

corresponds to the axis along which Δy and $\Delta\theta$ were measuring displacement. Therefore, Fig. 5 indicates that changes in PEP were related to displacement along the major axis of the manifold in this study.

The relationship between Δy and ΔPEP is further explored in Fig. 6(a), which shows a strong positive correlation resulting in an R^2 of 95.3% across all subjects. Correspondingly, Fig. 6(b) shows a strong positive correlation between $\Delta\theta$ and ΔPEP, resulting in an R^2 of 92.5% across all subjects. Building on these results, Fig. 6(c) reports the RMSE for estimating ΔPEP using the latent variables derived from ISOMAP and manifold approximation respectively using held-out cross validation. The median RMSE was lower for ISOMAP at 1.38 ms, though manifold approximation still estimated ΔPEP with a median RMSE of 2.45 ms. Prior literature in the field of PEP estimation from SCG has focused on estimating the precise timing of PEP rather than relative changes as was performed in this work. Placing the results of Fig. 6(c) into context, the RMSE for automated PEP estimation in prior studies has typically fallen between 9–12 ms, depending upon the method and reference [39], [40].

On the one hand, estimation of ΔPEP rather than PEP itself is a limitation of a manifold mapping approach compared to prior literature; however, this may in turn enable physiological monitoring in a morphology-free manner. Consider Fig. 4(d), which shows the SCG manifolds for all animal subjects on the same axes. Though the orientation of each manifold varied due to differences in morphology, the underlying dynamics which generate the manifold were consistent across subjects. This enabled consistent determination of displacement along the manifold despite its morphology-dependent position, as performed with
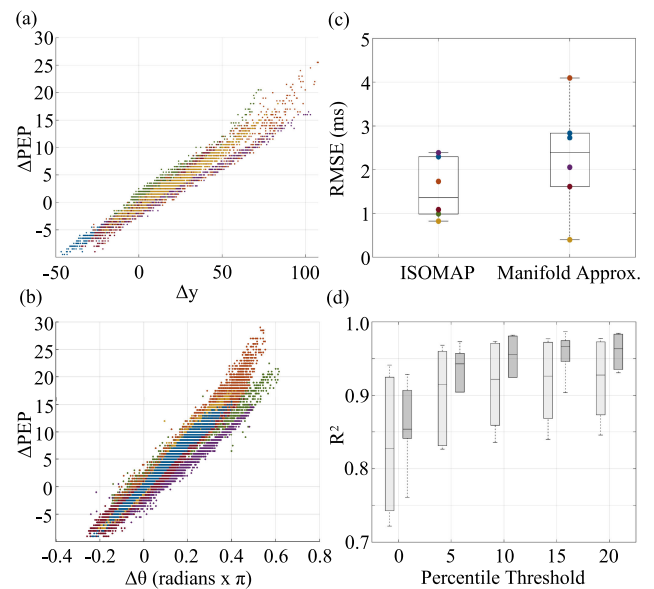

Fig. 6. (a) The latent variable Δy derived from ISOMAP plotted against ΔPEP. (b) The latent variable $\Delta\theta$ derived from manifold approximation plotted against ΔPEP. (c) Error in estimating ΔPEP using ISOMAP and manifold approximation, respectively. Colors in (a)–(c) correspond to animal-specific colors in Figs. 4(d) and 5. (d) The effect of the SQI percentile threshold on the R^2 between Δy and ΔPEP (dark gray) as well as $\Delta\theta$ and ΔPEP (light gray).

both ISOMAP and manifold approximation. In this manner, a shift in perspective from the time-domain to signal dynamics may be the key to unlocking morphology-free SCG analysis, enabling more robust processing.

These results have further implications which transcend PEP estimation with SCG signals. Namely, the observation of consistent low-dimensional manifold structure in SCG signals suggests that (1) these signals have low intrinsic dimensionality despite their observation in high-dimensional vector spaces; and (2) that the latent variables describing these intrinsic dimensions have consistent dynamics for the same physiological stimulus, in this case changes in blood volume due to exsanguination and fluid resuscitation. These observations may represent a shift in how we understand SCG signals: rather than focusing on time-domain features of these signals, data with such properties may be better understood in terms of their low-dimensional dynamics, which lack the stochasticity of signal morphology.

The SCG data forming the manifolds in Fig. 5 and the results in Fig. 6 were obtained during both exsanguination and fluid resuscitation. During this time, changes in PEP were encoded in the manifolds formed by the SCG signals, and hemorrhage-induced changes in this aspect of cardiomechanical function were thereby quantifiable via manifold mapping approaches. For this reason, these results demonstrate the clinical potential for reliable physiological estimation from SCG signals during trauma-induced hemorrhage and subsequent treatment. Namely, estimating indicators of cardiomechanical function such as PEP noninvasively may enable new clinical tools to allow health-care providers to manage trauma injury, serving as additional indicators of the severity of hemorrhage and the patients' response to fluid resuscitation. By estimating changes in PEP in a morphology-independent manner, these results represent an important step in addressing the major limitations preventing the ubiquitous application of SCG in clinical environments such as these.

B. Effect of the SQI on Manifold Mapping

The effect of increasing the SQI cutoff on manifold-derived estimation of ΔPEP is detailed in Fig. 6(d). As illustrated, the performance of both ISOMAP and manifold approximation improved as the cutoff was increased, an effect which diminished once a threshold of 10% had been reached. Fig. 3 serves as a representative example of why this was the case for ISOMAP: removing low-quality signals as defined by the SQI resulted in the emergence of the two-dimensional manifolds of Fig. 4, which could in turn be embedded more reliably in the two-dimensional output space $\mathscr{Y}$. Regarding the proposed manifold approximation, preserving points which better reflected the underlying rotational dynamics of the signal led to more accurate approximation of angular offsets.

Importantly, the low percentage threshold at which performance of these manifold mapping algorithms leveled off suggested only a minority of SCG points could not be described by a low-dimensional manifold structure. The implication of this observation is that the manifolds observed in Fig. 4 were not merely consequences of applying the SQI to inherently high-dimensional data; rather, the data itself was predominantly described by a low-dimensional manifold to begin with, with a minority of signal segments forming outliers. This supports the assertion that a low-dimensional manifold structure is intrinsic

to SCG signals and were not merely a consequence induced by the SQI itself. Conversely, this result highlights the importance applying signal quality indexing before searching for such structure in the data; as illustrated in Fig. 3, the presence of outliers may obscure the underlying manifold-level dynamics, possibly contributing to the historical difficulty in characterizing this behavior.

C. Study Limitations and Future Work

The current study focused on PEP estimation during trauma injury using an animal model, which limits the generalization of these results to a diverse array of possible applications in human subjects. Future studies should explore manifold mapping approaches for other interventions and for human subjects as well, though these studies should ensure that a reliable reference for PEP is used. Future work should also explore whether changes in other physiological indicators typically derived from SCG, such as LVET, may also be estimated using the latent variables of low-dimensional SCG manifolds. This would improve the utility of such methods for trauma injury triage, among other applications. As this work focused on PEP estimation during hemorrhage and resuscitation, future studies should further explore the potential role of manifold mapping in estimating the extent and severity of hemorrhage for possible application to the triage of trauma injury. While estimating the change in PEP may suffice for some methods, others may require direct estimation of PEP, highlighting a key limitation of the current work.

To optimize the accuracy of such methods, future work may explore a wide array of available methods for nonlinear dimensionality reduction and manifold mapping, many of which have lower complexity than ISOMAP. Such improvements may serve to reduce inter-subject variability, which as shown in Fig. 6(c) was an important limitation when the manifolds were rapidly approximated.

IV. CONCLUSION

The emergence of ubiquitous, wearable sensing technologies has the potential to revolutionize the treatment and management of cardiovascular disease. By integrating SCG sensors into such systems, one may assess mechanical aspects of cardiac function to obtain a holistic electromechanical view of heart health when paired with other sensors. This is especially useful in the case of trauma injury, where assessing cardiomechanical function may enable new clinical tools for managing hemorrhage and preventing hypovolemic shock.

Toward this goal, this study examined how PEP may be estimated in the context of hemorrhage and fluid-resuscitation using SCG signals in a manner that is abstracted from the time-domain, addressing a significant challenge in SCG processing. Importantly, the observation that SCG signals exhibit a consistent topological structure during hemorrhage and resuscitation suggests that although these signals may exhibit morphological heterogeneity, signal dynamics are preserved and may thereby lead to robust, consistent methods of physiological inference.

Though this dynamics-based approach enables the estimation of changes in PEP in lieu of PEP itself, elucidating the manifold

structure of these signals represents a significant advancement in the field of SCG processing. Ultimately, analysis methods which harness the intrinsic, underlying behavior of these signals may better bridge the gap between the laboratory and clinical practice, enabling the development of robust clinical tools in the fight against trauma injury and heart disease.

ACKNOWLEDGMENT

REFERENCES

[1] B. Bozhenko, "Seismocardiography–A new method in the study of functional conditions of the heart," *Terapevticheskii Arkhiv*, vol. 33, pp. 55–64, 1961.

[2] O. T. Inan *et al.*, "Ballistocardiography and seismocardiography: A review of recent advances," *IEEE J. Biomed. Health Informat.*, vol. 19, no. 4, pp. 1414–27, Jul. 2015.

[3] R. Crow *et al.*, "Relationship between seismocardiogram and echocardiogram for events in the cardiac cycle," *Amer. J. Noninvasive Cardiol.*, vol. 8, no. 1, pp. 39–46, 1994.

[4] K. Sørensen *et al.*, "Definition of fiducial points in the normal seismocardiogram," *Scientific Rep.*, vol. 8, no. 1, 2018, Art. no. 15455.

[5] M. Di Rienzo *et al.*, "Wearable seismocardiography: Towards a beat-by-beat assessment of cardiac mechanics in ambulant subjects," *Auton. Neurosci.*, vol. 178, pp. 50–59, 2013.

[6] M. Etemadi and O. T. Inan, "Wearable ballistocardiogram and seismocardiogram systems for health and performance," *J. Appl. Physiol.*, vol. 124, no. 2, pp. 452–461, 2018.

[7] K. Lee *et al.*, "Mechano-acoustic sensing of physiological processes and body motions via a soft wireless device placed at the suprasternal notch," *Nature Biomed. Eng.*, vol. 4, no. 2, pp. 1–11, 2019.

[8] O. T. Inan *et al.*, "Novel wearable seismocardiography and machine learning algorithms can assess clinical status of heart failure patients," *Circ Heart Fail*, vol. 11, no. 1, 2018, Art. no. e004313.

[9] C. Yang and N. Tavassolian, "Pulse transit time measurement using seismocardiogram, photoplethysmogram, and acoustic recordings: Evaluation and comparison," *IEEE J. Biomed. Health Informat.*, vol. 22, no. 3, pp. 733–740, May 2017.

[10] C. Poon and Y. Zhang, "Cuff-less and noninvasive measurements of arterial blood pressure by pulse transit time," in *Proc. IEEE Eng. Med. Biol. 27th Annu. Conf.*, 2006, pp. 5877–5880.

[11] R. A. Wilson *et al.*, "Diagnostic accuracy of seismocardiography compared with electrocardiography for the anatomic and physiologic diagnosis of coronary artery disease during exercise testing," *Amer. J. Cardiol.*, vol. 71, no. 7, pp. 536–545, 1993.

[12] K. Tavakolian *et al.*, "Precordial vibrations provide noninvasive detection of early-stage hemorrhage," *Shock*, vol. 41, no. 2, pp. 91–96, 2014.

[13] D. S. Kauvar and C. E. Wade, "The epidemiology and modern management of traumatic hemorrhage: US and international perspectives," *Crit. Care*, vol. 9, no. 5, pp. S1–S9, 2005.

[14] D. S. Kauvar, R. Lefering, and C. E. Wade, "Impact of hemorrhage on trauma outcome: An overview of epidemiology, clinical presentations, and therapeutic considerations," *J. Trauma Acute Care Surgery*, vol. 60, no. 6, pp. S3–S11, 2006.

[15] B. J. Eastridge, J. B. Holcomb, and S. Shackelford, "Outcomes of traumatic hemorrhagic shock and the epidemiology of preventable death from injury," *Transfusion*, vol. 59, no. S2, pp. 1423–1428, 2019.

[16] G. S. Chan *et al.*, "Change in pulse transit time and pre-ejection period during head-up tilt-induced progressive central hypovolaemia," *J. Clin. Monitor. Comput.*, vol. 21, no. 5, pp. 283–293, 2007.

[17] A. Taebi *et al.*, "Recent advances in seismocardiography," *Vibration*, vol. 2, no. 1, pp. 64–86, 2019.

[18] A. Taebi and H. Mansy, "Effect of noise on time-frequency analysis of vibrocardiographic signals," *J. Bioeng. Biomed. Sci.*, vol. 6, no. 4, 2016.

[19] H. Ashouri, S. Hersek, and O. T. Inan, "Universal pre-ejection period estimation using seismocardiography: Quantifying the effects of sensor placement and regression algorithms," *IEEE Sensors*, vol. 18, no. 4, pp. 1665–1674, Feb. 2017.

[20] J. B. Tenenbaum, "Mapping a manifold of perceptual observations," in *Proc. Adv. Neural Inf. Process. Syst.*, 1998, pp. 682–688.

[21] S. W. Bishnoi *et al.*, "All-optical nanoscale ph meter," *Nano Lett.*, vol. 6, no. 8, pp. 1687–1692, 2006.

[22] P. P. Lelovas, N. G. Kostomitsopoulos, and T. T. Xanthos, "A comparative anatomic and physiologic overview of the porcine heart," *J. Amer. Assoc. Laboratory Animal Sci.*, vol. 53, no. 5, pp. 432–438, 2014.

[23] C. Tei *et al.*, "Noninvasive doppler-derived myocardial performance index: Correlation with simultaneous measurements of cardiac catheterization measurements," *J. Amer. Soc. Echocardiogr.*, vol. 10, no. 2, pp. 169–178, 1997.

[24] W. Grossman, *Grossman's Cardiac Catheterization, Angiography, and Intervention*. Philadelphia, PA, USA: Lippincott Williams & Wilkins, 2006.

[25] A. C. Ertl, A. Diedrich, and S. R. Raj, "Techniques used for the determination of blood volume," *Amer. J. Med. Sci.*, vol. 334, no. 1, pp. 32–36, 2007.

[26] L. Yao *et al.*, "Evans blue dye: A revisit of its applications in biomedicine," *Contrast Media Mol. Imag.*, vol. 2018, 2018.

[27] C. Hinojosa-Laborde *et al.*, "Validation of lower body negative pressure as an experimental model of hemorrhage," *J. Appl. Physiol.*, vol. 116, no. 4, pp. 406–415, 2013.

[28] R. Mukkamala *et al.*, "Toward ubiquitous blood pressure monitoring via pulse transit time: Theory and practice," *IEEE Trans. Biomed. Eng.*, vol. 62, no. 8, pp. 1879–1901, 2015.

[29] M. D. Seery *et al.*, "Preejection period can be calculated using R peak instead of q," *Psychophysiology*, vol. 53, no. 8, pp. 1232–1240, 2016.

[30] D. B. Newlin and R. W. Levenson, "Pre-ejection period: Measuring beta-adrenergic influences upon the heart," *Psychophysiology*, vol. 16, no. 6, pp. 546–552, 1979.

[31] M. A. Van Eijnatten *et al.*, "Comparison of cardiac time intervals between echocardiography and impedance cardiography at various heart rates," *J. Elect. Bioimpedance*, vol. 5, no. 1, pp. 2–8, 2019.

[32] P. Kh Dehkordi *et al.*, "Comparison of different methods for estimating cardiac timings: A comprehensive multimodal echocardiography investigation," *Frontiers Physiol.*, vol. 10, p. 1057, 2019.

[33] J. Zia *et al.*, "A unified framework for quality indexing and classification of seismocardiogram signals," *IEEE J. Biomed. Health Inform.*, vol. 24, no. 4, pp. 1080–1092, Apr. 2020.

[34] P. Senin, "Dynamic time warping algorithm review," *Inf. Comput. Sci. Dept. Univ. Hawaii at Manoa Honolulu, USA*, vol. 855, pp. 1–23, 2008.

[35] J. A. Lee and M. Verleysen, *Nonlinear Dimensionality Reduction*. Berlin, Germany: Springer Science & Business Media, 2007.

[36] R. W. Floyd, "Algorithm 97: Shortest path," *Commun. ACM*, vol. 5, no. 6, p. 345, 1962.

[37] J. Wang, *Geometric Structure of High-Dimensional Data and Dimensionality Reduction*. Berlin, Germany: Springer, 2012.

[38] W. J. Vincent and J. P. Weir, *Statistics in Kinesiology*, 4th ed. Champaign, IL, USA: Human Kinetics, 2012.

[39] M. M. H. Shandhi *et al.*, "Performance analysis of gyroscope and accelerometer sensors for seismocardiography-based wearable pre-ejection period estimation," *IEEE J. Biomed Health Inform*, vol. 23, no. 6, pp. 2365–2374, Nov. 2019.

[40] P. Dehkordi *et al.*, "Estimation of cardiac time intervals from the mechanical activity of the heart using machine learning," *Computing*, vol. 46, pp. 1–4, 2019.